Check for updates

Proceedings of ASME Turbo Expo 2014: Turbine Technical Conference and Exposition
GT2014
June 16 – 20, 2014, Düsseldorf, Germany

GT2014-26007

Downloaded from https://asmedigitalcollection.asme.org/GT/proceedings-pdf/GT2014/45622/V02CT38A027/4228507/v02ct38a027-gt2014-26007.pdf by ETH Zuerich user on 17 October 2019

AERODYNAMIC ROBUSTNESS OF END WALL CONTOURING AGAINST RIM SEAL PURGE FLOW

K. Regina[1], A. I. Kalfas[2], R. S. Abhari[1], A. Lohaus[3], S. Voelker[4], T. auf dem Kampe[4]

[1] Laboratory for Energy Conversion, Dept. of Mechanical and Process Engineering, ETH Zurich, Switzerland
[2] Dept. of Mechanical Engineering, Aristotle University of Thessaloniki, 54124 Thessaloniki, Greece
[3] SIEMENS Energy Inc., Orlando, USA
[4] SIEMENS AG, Muelheim an der Ruhr, Germany

ABSTRACT

In the present study, the results of an experimental investigation are presented, which have been undertaken in the axial turbine facility LISA at ETH Zurich. The two test configurations consist of a one-and-a-half stage, unshrouded, highly loaded axial turbine with 3-dimensionally shaped blading representative of modern high pressure gas turbines. The two test configurations differ in the hub end walls: while one design has cylindrical end walls, the other design features non-axisymmetric end wall contouring (EWC).

Both turbine designs have not been especially designed for the unsteady and complex interaction mechanisms of the hub rim seal purge flow with the main annulus flow. However, these turbine designs have been subject to measurements without (nominal) and with purge flow (0.8% of the main mass flow) with the purpose of studying the aerodynamic robustness of the performance of the stages with respect to the rim seal purge flow. In order to further analyze the robustness of both turbine designs, also measurements at off-design conditions have been taken.

The steady and unsteady aerodynamic effects are measured, respectively, with pneumatic probes as well as with the in-house developed and manufactured Fast Response Aerodynamic Probe (FRAP) technology. With the aim of evaluating the aerodynamic performance and robustness of the end wall design, the one result of the experimental investigation is the quantification of the sensitivity of the stage efficiency with respect to the case with and without purge flow for both turbine designs. By means of the analysis of the time-resolved flow field and characterization of the secondary flow features, their reaction to the presence of purge flow is highlighted and used as an explanation for the efficiency deficits caused by the purge flow.

The measurements show a benefit in stage efficiency of +0.2% by using the end wall contouring in the nominal case, confirming the design intention and effectiveness of the contoured end walls. However, the beneficial impact of the end wall contouring is taken back by a higher sensitivity of the stage efficiency with respect to the purge flow, which causes the efficiency benefit to vanish with the investigated purge flow injection rate of 0.8%. The off-design measurements show that also the sensitivity of the stage with end wall contouring with respect to the reduction of stage loading factor is by 1/3 higher than the one of the cylindrical end walls.

The measurements imply that the cost of higher stage efficiency at nominal conditions by the use of end wall contouring is paid with a higher sensitivity of the stage to changes in the rotor incoming flow field and thus with a lower aerodynamic robustness of the turbine design.

INTRODUCTION

In modern gas turbines, non-axisymmetric end wall contouring (EWC) is used as a successful design tool in order to influence the static pressure field in the passage between adjacent airfoils. By guiding the secondary end wall flows while these are convected through the passage, non-axisymmetric end wall contouring can reduce the penetration of the end wall loss cores into the main passage thus enhancing the aerodynamic performance.

A characteristic feature for ensuring the mechanical integrity of modern gas turbines is the use of purge flow, which is injected through stator/rotor rim seal gaps from the hub in order to prevent the ingestion of hot gases from the main flow

Copyright © 2014 by Siemens Energy, Inc.

into the disk cavities between the rotor components and the stator components. However, the complex mixing mechanisms of the purge flow and the main flow result in a detrimental impact on the turbine performance which is caused by the alteration of the behavior of the secondary flows of the hub.

One first main category of studies presented in this topic deals with the design intentions and the impact of the use of non-axisymmetrically contoured end walls on the turbine flow field. These studies prove that non-axisymmetric end wall contouring can be used as a tool for improving turbine performance through reduction of secondary flows. On a scaled model of an high pressure turbine of the Rolls-Royce Trent 500 engine, Rose et al. [1] have experimentally quantified the efficiency improvement due to EWC to be about 0.6%. For the IP turbine of the same engine model, Harvey et al. [2] have found an efficiency benefit of 0.9%. However, they report that these efficiency differences are dependent on the operating point of the turbine. In a later publication, also Snedden et al. [3] indicate the dependence of the efficiency benefit due to EWC on the operating point. There, the efficiency improvement decreases with increasing loading of the stage from 0.9% to 0.3% throughout the loadings tested. Although contouring is only applied on the hub end walls an impact on the tip leakage flow is also reported but not fully understood [3]. For a turbine stage of similar blading than in the present study, Schüpbach et al. [4] have measured a stage efficiency benefit of 1% due to EWC, where most of the improvement has been found to originate in the nozzle guide vane. In a recent study, Miyoshi et al. [5] focused their experimental investigations on the effect of contouring the stator end walls of an high pressure turbine stage on the stage performance. The authors report on an unexpected impact of the end wall contouring on the midspan profile losses of the vane, which is not fully understood. In another recent study, Dunn et al. [6] confirm the previous findings of Snedden et al. [3], where the hub end wall contouring had impacted the tip leakage flow. However, the authors do not conclude on a final mechanism for this effect.

A second main category of publications addresses the impact of purge flow injection on the main annulus flow of the turbine and highlights the mixing mechanisms of the flows. Several experimental studies of purge flow interaction mechanisms on both high and low pressure turbine stages report a highly unsteady entrainment mechanism of cavity fluid into the hub passage vortices of the rotors and stators, such as Hunter and Manwaring [7] or Schrewe et al. [8] for different 2-stage low pressure turbines, Jenny et al. [9] for a 1.5-stage low pressure turbine and Ong et al. [10] or Schüpbach et al. [11] for different high pressure turbine stages. However, different publications address the dependence of the purge flow effects on different elements of the turbine design. Mc. Lean et al. [12] analyzed different injection configurations on a single high pressure stage and found the efficiency sensitivities to the amount of purge flow injected to be strongly dependent on the type of injection. Based on investigations with a single stage turbine with different circumferential injection angles, Reid et al. [13] warn when it comes to generalizing the findings to other turbines. In a recent publication, Regina et al. [14] experimentally show that the magnitude of the purge flow impact on the flow field and its spanwise extent is strongly dependent on the aerodynamic design of the stages even for high pressure stages under same operating conditions and with the same aspect ratio. Different studies attribute the impact of the purge flow to different effects: For a transonic single high pressure stage, Paniagua et al. [15] attributed the increased penetration depth of the rotor hub passage vortex to the lower temperature of the purge flow as compared to the main annulus flow. Ong et al. [10] attribute the strengthening of the rotor HPV and its increased penetration depth with purge flow to the negative incidence coming along with the purge flow. Regina et al. [16] report a trendwise correlation of the purge flow induced increase in strength and penetration depth of the rotor HPV with the induced local increase of stage flow factor as more mass flow is pushed through the lower spans when purge flow is introduced.

In the recent past some publications have started to address the combined effects and interaction mechanisms of both contoured end walls and purge flow on the flow field of the turbine. Schüpbach et al. [17] have experimentally quantified the sensitivity of the stages with respect to purge flow for different EWC designs and found that they can differ by a factor of 2. They also report on CFD failing to predict these efficiency trends, since the efficiency differences between the end wall designs at a fixed injection rate as well as the spread of the sensitivities of the end wall designs with respect to the purge flow was underpredicted by the CFD models. Based on measurements in an axial research turbine, Turgut and Camci [18] have found the EWC to be beneficial for the losses upstream of the location where the purge flow is injected. However, this benefit could not persist downstream of the location where the injection of the purge flow takes place. Rakenius et al. [19] have experimentally shown a reduction by about 1/3 in sensitivity of a stage with EWC with respect to purge flow when compared to the same stage without end wall contouring.

In order to better understand the highly unsteady interaction mechanisms with the end wall contouring, the present work experimentally quantifies the sensitivity of the isentropic total-to-total efficiency of two high work turbines with different hub end wall designs to the amount of mass fraction of purge flow injected from the rotor upstream rim seal. Since the airfoils and end walls were not especially designed to handle the detrimental and unsteady interaction mechanisms of the purge flow, the current work aims to characterize the robustness of the designs when subject to the off-design effects inherent to the purge flow injection as well as to identify and better understand the interaction mechanisms of contoured end walls and purge flow injection.

Downloaded from https://asmedigitalcollection.asme.org/GT/proceedings-pdf/GT2014/45622/V02CT38A027/4228507/v02ct38a027-gt2014-26007.pdf by ETH Zuerich user on 17 October 2019

Copyright © 2014 by Siemens Energy, Inc.

EXPERIMENTAL METHOD

The current experimental study was performed in the research axial turbine rig called "LISA" in the Laboratory for Energy Conversion at ETH Zurich. The test rig was subsequently assembled with two one-and-a-half stages with shroudless rotors, which are representative for modern high work turbines. Whereas one stage had cylindrical end walls at hub and tip, the other stage design featured contoured hub end walls at all three blade rows. The focus of the present paper lies in the analysis of the flow field of the first stage.

Research Turbine Facility

The research turbine facility is composed of a quasi-closed air loop which includes a single stage centrifugal compressor delivering the flow, a two stage water-to-air heat exchanger controlling the turbine inlet temperature and a calibrated venturi nozzle for accurate mass flow measurements. A schematic of the rig is depicted in Figure 1.

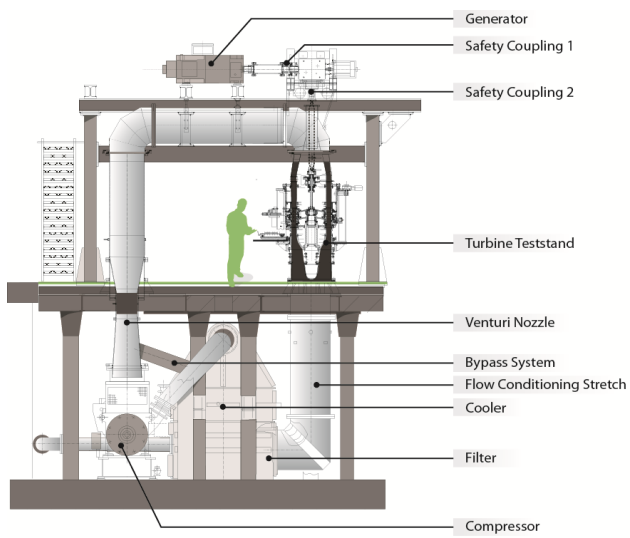

Figure 1: Schematics of the test facility "LISA" at ETH Zurich

Upstream of the test section of the turbine, there is a 3-m-long flow conditioning duct in order to ensure flow field homogeneity at the turbine's inlet. For additionally reducing the significance of any remaining flow non-uniformities from upstream, the flow undergoes an acceleration ahead of the turbine. At the exit of the turbine test section, the air loop is open to atmospheric conditions. A DC generator converts and feeds the turbine's power into the electrical grid and controls the rotational speed with an indicated accuracy of ±0.02% (±0.5rpm). The total inlet temperature $T_{0,in}$ is controlled by the water-to-air heat exchanger to an accuracy of ±0.3K. A torquemeter is used for torque measurements on the rotor shaft. Since the pressure ratio of the compressor is limited to $\Pi_{c,max}$ = 1.5, it is necessary to operate a tandem deswirl vane arrangement to recover the static pressure at the exit of the second stator back to the ambient level in order to reach the intended pressure ratio of the turbine of $\Pi_{1.5}$ = 1.65. The shroudless rotors have a nominal tip gap of 1% of the span and the variation of the tip gap between different assemblies of the turbine test section is less than 1% of the tip gap, which ensures good repeatability. At the exit of the first stator the flow is compressible with an averaged Mach number of 0.53.

The present turbine configurations are derived from and belong to the blade family of the turbine design extensively presented by Behr et al. [20]. The most salient differences are an increased blade row spacing between the first stator and the rotor, an increased axial gap at the exit of the hub cavity, from where the purge flow is injected, as well as a new 3D airfoil design.

Operating Conditions

During the measurements the turbine's 1.5 stage total-to-static pressure ratio is kept constant at $\Pi_{1.5}$ = 1.65. By doing so, the changes in the ambient pressure on different days are accounted for. With the same purpose, the pressure values used in this paper are non-dimensionalized by the respective inlet stagnation pressure. The main operating parameters are summarized in Table 1.

Table 1: Operating conditions and geometrical characteristics

Pressure ratio $\Pi_{1.5}$	1.65 ± 0.4 %	[–]
Inlet total temperature $T_{0,in}$	327.9 ± 0.3	$[K]$
Capacity $\frac{\dot{m}\sqrt{T_{0,in}}}{p_{0,in}}$	152.7 ± 0.1	$\left[\frac{kg \cdot K^{1/2}}{s \cdot bar}\right]$
Non-dimensional speed $\frac{N}{\sqrt{T_{0,in}}}$	2.49 ± 0.05	$\left[\frac{rps}{K^{1/2}}\right]$
Mach nr (S1 ex / R ex / S2 ex)	0.53 / 0.26 / 0.48	[–]
Blade count (S1 / R / S2)	36 / 54 / 36	[–]
Aspect ratio (S1 / R / S2)	0.87 / 1.17 / 0.82	[–]

The rim seal purge flow is continuously injected from the rotor upstream stator/rotor cavity along the full annulus. It is an off-take from the primary air loop upstream of the flow conditioning stretch and is measured by means of a standard nozzle. The bypassed air passes a plenum and is fed through different nozzle guide vanes into the cavity underneath the NGV hub platform, labeled as B in Figure 2 left, which shows a schematic of the purge flow path.

After the purge flow enters the cavity underneath the stator platform, there are two paths, which are indicated by dotted arrows in Figure 2: One path is through the rotor upstream rim seal into the main flow and is labeled as P in Figure 2 left. Another path, termed secondary mass flow and labeled as S in Figure 2, is ejected through the drum into the atmosphere, after being measured in an additional standard nozzle. Because the pressure difference across the rotor downstream rim seal is

Downloaded from https://asmedigitalcollection.asme.org/GT/proceedings-pdf/GT2014/45622/V02CT38A027/4228507/v02ct38a027-gt2014-26007.pdf by ETH Zuerich user on 17 October 2019

Copyright © 2014 by Siemens Energy, Inc.

controlled to be zero during the experiments, the net mass flow through the downstream rim seal gap can be assumed to be zero. As a consequence, the mass flow P eventually injected into the main flow can be calculated as the difference between the measured bypass mass flow B and the measured secondary mass flow S. A close-up view of the rim seal geometry used in the present investigations is depicted on Figure 2 right. The characteristic geometrical details are a gap width of 20% of the axial chord of the first stator and a platform chamfer angle of 45° and are given in Figure 2.

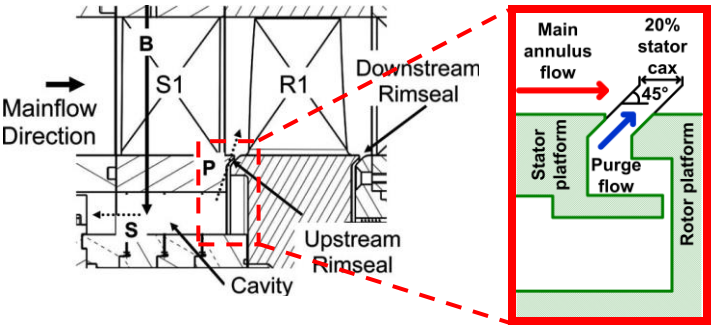

Figure 2: Schematics of the purge flow path on the left [4] (not to scale) and details of upstream rim seal on the right

In agreement with previous investigations, the injection levels were defined by means of the injection rate (IR) defined by Equation 1.

$$IR = \frac{\dot{m}_B - \dot{m}_S}{\dot{m}_{MAIN}} \cdot 100 \qquad (1)$$

The present tests have been performed with IR1=0%, IR2=0.8% and IR3=1.2%, which are considered to be representative for real engine conditions.

Measurement Technology

For the steady flow field measurements at the exit of the rotor, a miniature cobra-head five-hole probe (5 HP) with a tip diameter as small as 0.9mm is used, whereas at the inlet of the rotor, a pneumatic miniature four-hole probe (4 HP) with a cylindrical head and a diameter of 1.8mm is used.

For the unsteady flow field measurements, the Fast Response Aerodynamic Probe (FRAP) is used. This probe technology was developed in-house at the LEC at ETH Zurich and more details on the probe and the measurement technique are presented in depth in Kupferschmied et al. [21] and Pfau et al. [22]. By means of FRAP measurements, unsteady flow features with frequencies of up to 48kHZ can be captured based on measurements including the total and static pressures, as well as flow yaw and pitch angles, from where the velocity components and further flow quantities are derived. The frequency bandwidth of the temperature signal is limited to a frequency of 10Hz. However, the influence of the measured temperature on the velocity is judged to be very modest. The tip of the FRAP has a diameter of 1.8mm and contains two miniature silicon piezo-resistive pressure transducers. In order to measure the 3-dimensional, time-resolved flow properties, the probe is operated in a virtual-4-sensor mode. The data is acquired at a sampling rate of 200kHz over a period of time of 2s and the post-processing is done for three consecutive rotor pitches. With the given sampling rate and the present test cases, the flow field of one rotor passage is resolved with 82 points. The typical measurement uncertainties, which are achieved with the FRAP and with the 5 HP at the rotor exit measurement plane, are given in Table 2 for a calibration range of ±24° in the yaw angle and ±20° in the pitch angle. The relative uncertainties of the total and static pressures are given as a percentage of the dynamic head.

Table 2: Uncertainty bandwidth of FRAP and 5 HP

	Yaw angle	Pitch angle	p_t	p_s
FRAP	0.62°	0.64°	2.8%	3.7%
5 HP	0.34°	0.40°	1.9%	2.2%

The measurement data presented in this paper were acquired at two different axial locations in the turbine test section by traversing the probe in radial and circumferential direction. The first traversing plane is labelled with "R in" and is located upstream of the rotor at a distance between the plane and the blade leading edge at midspan of 14% of the rotor axial chord. This axial location coincides with the rotor hub platform leading edge, i. e. with the rotor sided edge of the rim seal gap through which the purge flow is injected. The second traverse plane, labelled with "R ex" is located downstream of the rotor at a distance between the plane and the rotor trailing edge of 13% of the rotor axial chord. The spatial resolution of the measurement grid at these traversing planes consisted of 38 points in radial and 41 points in circumferential direction covering one stator pitch. The circumferential points were equally spaced whereas the radial points were clustered near the end walls. In order to ensure the integrity of the probes, a safety distance to the hub end walls was kept and the lowest accessible spanwise position was approximately 6% span.

AIRFOIL AND END WALL CONTOURING DESIGN

The airfoils and end walls exposed to the off-design effects associated with the purge flow injection are characterized in the following section.

Airfoil Design

As mentioned previously, the airfoils studied in this paper are derived from the turbine studied by Behr et al. [20]. In addition to changes in axial spacing of the rows for purposes of altering the vane-rotor purge leakage, the airfoils themselves were also modified.

The profiles of the vanes were essentially unchanged, but the stacking lines were modified to have lean, bow, sweep and stagger angles that varied continuously along the airfoil span. The stacking of the rotor was essentially unchanged, but the

Downloaded from https://asmedigitalcollection.asme.org/GT/proceedings-pdf/GT2014/45622/V02CT38A027/4228507/v02ct38a027-gt2014-26007.pdf by ETH Zuerich user on 17 October 2019

Copyright © 2014 by Siemens Energy, Inc.

profiles were modified along the pressure and suction sides. Capacities of each row were kept constant to preserve overall aerodynamic similarity to the basis design.

While some of these changes were made manually, most of the design was executed in a CFD-based optimization system. The system combines publically available meshing, CFD and optimization codes with Siemens proprietary scripting and geometry codes. The model used time-averaged simulations on block-structured grids, with efficiency as the target function.

In Figure 3 the tested rotor geometry as well as the midspan profile are depicted.

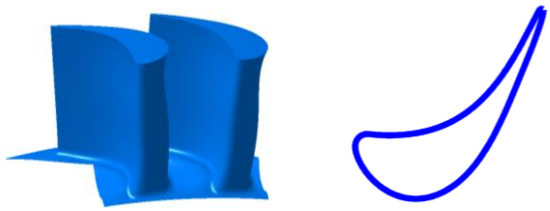

Figure 3: Tested rotor geometry isometric view (left) and profile at midspan (right)

End Wall Contouring Design

The contoured end wall designs were based on the optimized airfoils described above. With the exception of extending the airfoil radially in regions where the contoured end walls had a lower radius than the cylindrical end walls, no changes were made to the airfoil sections or stacking. A third end wall, on the hub of the second stator, was also designed and tested at the same time, but those results are not presented in this publication.

Consistent with other publications on the topic, the end walls are defined by a surface lofted through a series of curves that are parallel to each other in the circumferential direction. The underlying surface largely follows the outline of the airfoils, with two adjacent end wall surfaces not meeting underneath most of the airfoil. A Fourier series expansion was used to define the circumferential curves on the vane end wall, while b-splines were used for the rotor. The number of parameters and constraints used to define the circumferential curves is independent at each axial station, giving the designer a great deal of flexibility. For example, periodicity between adjacent end walls can be enforced where needed, while also achieving complex shaping at critical locations between adjacent airfoils. A total of 26 and 41 parameters were used to define the vane and rotor end walls, respectively.

Starting from these geometric parameterizations, the specific designs were then created within an automatic CFD-based optimization system similar to that used for the airfoils. Due to concerns over achieving consistent convergence of the CFD model, the cavity and purge flow were not included during the optimization process. The target function was 1.5-stage efficiency. One end wall was optimized at a time, with the final optimization of each row being carried out with a (fixed) intermediate design on the other rows.

At the end of the optimization phase, the capacity of each row was matched to the cylindrical case by adjusting the end wall surfaces instead of re-staggering the airfoils. A final assessment of the design in a higher-resolution CFD model predicted a 0.24% increase in 1-stage efficiency over the cylindrical end walls in the case without purge flow.

The contour map of the elevation of the end walls of the first stage are shown in Figure 4.

RESULTS AND DISCUSSIONS

The main purpose of the current investigations is not the validation of the EWC methods but instead the aerodynamic robustness study against the off-design effects introduced by the purge flow and more specifically the identification of the origin of performance changes. Thus, the focus of the results discussion is put on the effect of the purge flow on the two designs, rather than explaining the performance changes due to end wall contouring only.

Stage performance evaluation of EWC

First of all, the detrimental impact of the purge flow injection on the performance of both stages shall be quantified by means of the isentropic total-to-total efficiency, which is used as defined in Equation 2 and in which the enthalpy drop of the purge flow is also taken into account.

$$\eta_{tt} = \frac{\dfrac{\omega \cdot M}{m_{MAIN} \cdot c_p \cdot T_{0,in}}}{1 - \left(1 - \dfrac{IR}{100}\right) \cdot \left(\dfrac{p_{0,R_{ex}}}{p_{0,in}}\right)^{(\gamma-1)/\gamma} - \dfrac{IR}{100} \cdot \left(\dfrac{p_{0,R_{ex}}}{p_{0,cav}}\right)^{(\gamma-1)/\gamma}} \qquad (2)$$

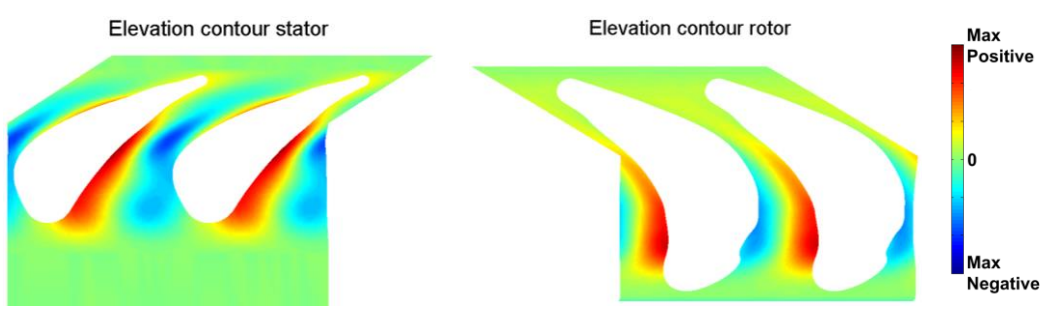

Figure 4: Elevation contour diagram of the contoured end walls

Copyright © 2014 by Siemens Energy, Inc.

Downloaded from https://asmedigitalcollection.asme.org/GT/proceedings-pdf/GT2014/45622/V02CT38A027/4228507/v02ct38a027-gt2014-26007.pdf by ETH Zuerich user on 17 October 2019

In the post-processing of the measurement data, Equation 2 is evaluated at each point in the measurement grid of the 5 HP. There, only the total pressure at the exit of the stage $p_{0,Rex}$ is obtained from measurements of the traversing probe whereas the rest of the quantities are acquired with different types of instrumentation fixedly installed in the test section. The rotational speed ω and the torque M are measured by a shaft mounted torquemeter, while the main mass flow rate m_{MAIN} is measured by the previously mentioned venturi nozzle at the inlet of the turbine. Ahead of the turbine test section, the turbine inlet total pressure $p_{0,in}$ is measured by six pitot tubes and the turbine inlet temperature $T_{0,in}$ by three resistance thermometers distributed along the circumference. For the total pressure of the purge flow in the cavity $p_{0,cav}$, end wall tappings are used, since the low velocities in the cavity plenum yield a negligible dynamic head.

By averaging over the entire measurement grid, the integral values of the stage efficiency are obtained and summarized in Figure 5, where the values are referenced to the efficiency of the test case with cylindrical end walls and with zero net purge flow. For the probe used, the turbine operating point and the calibration model applied, the derived total-to-total stage efficiencies have an absolute standard uncertainty of ± 0.18%. The corresponding error bars are also included in Figure 5. In general, and since the measurement grid needs to leave a gap of approximately 3.5% span from the rotating end wall for ensuring probe integrity, the measurements exclude the impact of the near hub flow. By doing so, a small increase or over estimation of efficiency is introduced into the measurements, which is judged to be negligible and does not impact relative comparisons between test cases and will not be further considered.

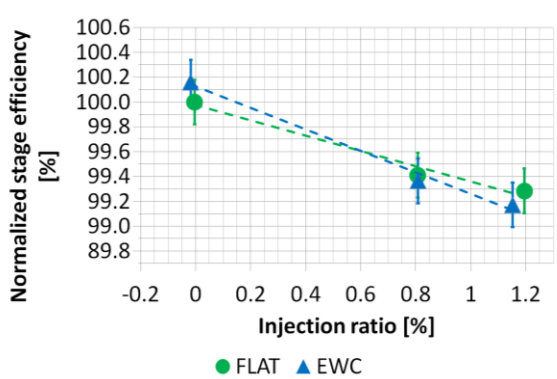

Figure 5: Sensitivity of the total-to-total stage efficiency with respect to purge flow for both tested end walls

The first important result to mention is the efficiency improvement due to the use of non-axisymmetric end wall contouring at zero net purge flow injection. There, an efficiency benefit of about +0.2% has been measured for the EWC case with respect to the cylindrical case. These experimental results agree extraordinary well with the predicted efficiency increase of +0.24% at the nominal operating condition, and therefore prove the functionality and the effectiveness of the end wall contouring design.

However, the second important result is that the efficiency benefit of the EWC case vanishes if purge flow is introduced and the EWC is even disadvantageous at the higher injection rate tested. This is a result of a higher sensitivity of the EWC case with respect to the rim seal purge flow injection. Based on a linear regression, the sensitivity increased by more than 1/3, from -0.62% per percent of injected mass flow in the case of the cylindrical end walls to -0.87% per percent of injected mass flow for the case of the contoured end walls.

In the rest of the paper, the 3D and 4D (time-resolved) flow field measurements will be analyzed in order to highlight where these results originate from.

Rotor exit flow field

For the characterization of the rotor exit flow field, first the efficiency differences between the end wall cases shall be looked at in terms of the circumferentially mass weighted distribution. This is shown in Figure 6, where the radial profiles are plotted for the case without net purge flow on top and with the middle injection rate at bottom. For each injection rate, also the difference of the efficiency of the contoured end wall to the efficiency of the cylindrical end wall is depicted in Figure 6.

When comparing both diagrams of Figure 6, it can be concluded that the influence of the end wall contouring reaches until midspan, regardless of the presence or absence of the purge flow injection.

More specifically, at zero net purge flow, the above given efficiency benefit of about +0.2% can be identified to be a result from the combination of a reduced intensity of the hub loss core at about 15%-20% span together with a lower penetration depth of the hub loss core away from the end wall reduced by about 4% span. This proves that the end wall contouring meets the design intent of keeping the lift-off of the hub vortices smaller.

Furthermore, at the middle injection rate of IR2=0.8%, one observes that although the integral value over the entire measurement grid remains unchanged, the radial distribution does change due to the contouring of the end walls. In time-average, the shift in radial location of the loss core peaks due to the contouring remains about 4% span and is unaffected by the purge flow injection, which is still a benefit originating from the end wall contouring. However, a redistribution of mass flow must be taking place, such that more loss fluid is pushed towards midspan. This causes a reduction in stage efficiency from 30% until 50% span, where the contoured case shows a lower performance and which counterbalances the efficiency gain in the peak of the loss cores.

Downloaded from https://asmedigitalcollection.asme.org/GT/proceedings-pdf/GT2014/45622/V02CT38A027/4228507/v02ct38a027-gt2014-26007.pdf by ETH Zuerich user on 17 October 2019

Copyright © 2014 by Siemens Energy, Inc.

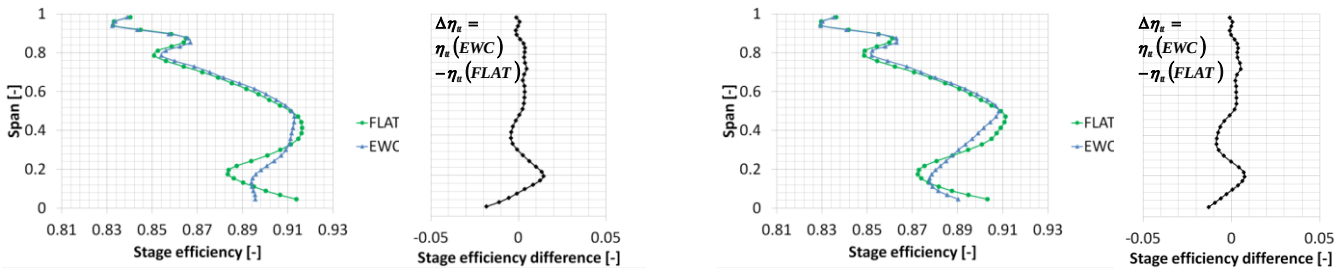

Figure 6: Time averaged and circumferentially mass weighted stage efficiency and stage efficiency differences for the case without purge flow (top) and for the case with IR2=0.8% purge flow (bottom)

Since the integral efficiency differences when comparing the end walls are in the range of the standard uncertainty of the measurement approach, additional repeatability measurements with the middle injection rate of IR2=0.8% have been performed for the case of the cylindrical and contoured end walls and are presented in Figure 7.

As can be concluded from Figure 7, the repeatability of the efficiency measurements is excellent and ensures a meaningful comparison between the different test cases, since the small differences in the radial distributions of each repetition set are well below the differences between the test cases throughout the entire span. Furthermore, the integral difference between the repetition measurements is as small as 0.02% for the cylindrical end walls and with 0.12% slightly larger in the contoured end wall test case. However, these values are smaller than the above quoted standard uncertainty by a factor of three and up to 18 for the contoured and cylindrical end wall test cases respectively.

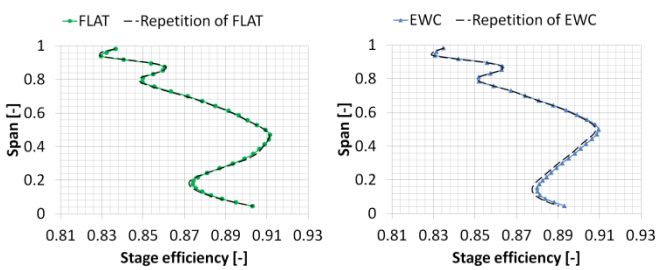

Figure 7: Time averaged and circumferentially mass weighted stage efficiency and repetition measurement for the middle IR2=0.8% for the cylindrical (left) and the contoured (right) end wall test case

The explanation of the trends captured by the steady pneumatic probe require the analysis of the 3D flow field and of the 4D measurements taken with FRAP.

For this purpose, the rms of the random part of the unsteady pressure signal as acquired with FRAP, which is a good indicator for unsteadiness and turbulence, is depicted in Figure 8. There, a snapshot in time of the time-resolved data is shown in the absolute frame of reference. The point in time corresponds to a specific blade-vane position, where the difference of radial penetration depth of the rotor HPV of two adjacent blade passages is large and was chosen to better visualize the periodic nature of the penetration depth of the rotor HPV.

The analysis of the instantaneous time-resolved data for further blade passing time points (not depicted here) shows that the vortex increases the penetration depth as it interacts with the secondary flows of the upstream stator. At the exit of the rotor, these features can still be tracked at a fixed circumferential position, and can be identified in Figure 8 as a region of high rms extending throughout the span at a circumferential position of about 0.7 stator pitch. Additionally to the impact of the stator secondary flows on the radial migration of the vortex, also an oscillation in circumferential direction is visualized in the above Figure 8, since the circumferential detachment of the vortex to the secondary flows induced by the trailing shed vorticity of the rotor blade is different for the two adjacent blade passages considered above and seen in Figure 8. Subsequently, the radial and circumferential location of the core of the vortex in the rotating frame of reference is periodically dependent on time (or on the blade-vane relative position) and the vortex describes an orbit in the rotating frame of reference.

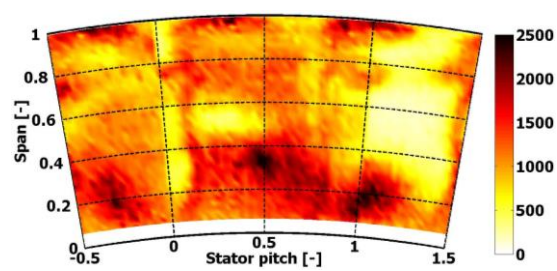

Figure 8: Instantaneous contour of rms(p_1') [Pa] at the rotor exit for the EWC case with the middle IR2=0.8%

Furthermore, the time-resolved periodic oscillation of the radial penetration depth of the rotor HPV is seen reflected in the rotor relative time averaged data. In order to visualize this, the time-averaged streamwise vorticity at the exit plane of the rotor is depicted in Figure 9 in the rotating frame of reference. The test case shown is the turbine with EWC without net purge flow injection on top and with the IR2=0.8% at bottom, in order to show the influence of the purge flow on the flow field of the contoured end wall test case.

Copyright © 2014 by Siemens Energy, Inc.

Downloaded from https://asmedigitalcollection.asme.org/GT/proceedings-pdf/GT2014/45622/V02CT38A027/4228507/v02ct38a027-gt2014-26007.pdf by ETH Zuerich user on 17 October 2019

The main effect of the purge flow injection on this test case is in good agreement with previous findings reported in literature: the most dominant effect of the purge flow is the interaction with the rotor hub passage vortex, making it stronger and with a larger area of influence. Another clear effect is seen on the trailing shed vorticity, which shows a vorticity orientation opposed to the one of the rotor HPV. For this region in the flow field, also a strengthening and enlargement of the area of influence is resulting from the purge flow injection.

However, another salient difference between both flow fields is the shape of the area of influence of the hub passage vortex and more specifically the peak intensity zone. It is clear that for the case without the purge flow, the time-averaged core has a more vertically oriented shape seen in the top contour diagram of Figure 9. This change in the time-averaged shape must be originated from a change in the unsteady behaviour of the orbit of the rotor HPV. The change in the time-averaged shape is seen to be a result from a stronger circumferential component of the periodically oscillating vortex centre, which is driven by the purge flow injection and which therefore causes the radial component, dominant in the case without net purge flow, to lose significance. This is also reflected in the circumferentially mass averaged streamwise vorticity, as depicted in Figure 10.

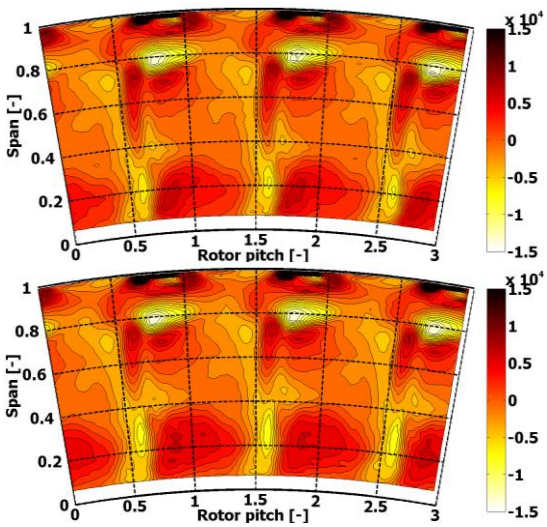

Figure 9: Time averaged streamwise vorticity [Hz] in the rotating frame of reference for the case without purge flow (top) and for the case with IR2=0.8% purge flow (bottom)

These findings are supported by the time-resolved measurements shown in Figure 11 for the IR2=0.8%. There, the span-time contour diagrams are shown for the cylindrical end walls on top and for the contoured end walls at bottom. The quantity depicted is again the rms of the random part of the pressure signal acquired by FRAP. The data comes from two radial traverses, which are half a stator pitch apart from each other. The main difference between these two traverses (in the absolute frame of reference) is the remaining unsteadiness from the upstream stator exit flow field. While the first traverse (left in Figure 11) is characterized by having a low interaction with the secondary flows of the first stator and low unsteady pressure fluctuations across the entire span, the second traverse (right in Figure 11) shows the highest interaction with those secondary flows and subsequently higher levels of unsteady pressure fluctuations throughout the span. These two circumferential locations also correspond to the locations where the centre of the rotor hub passage vortex shows the lowest spanwise migration on the left and the highest on the right. This highest penetration depth is characterized by a strong interaction with the secondary flows from the upstream vane.

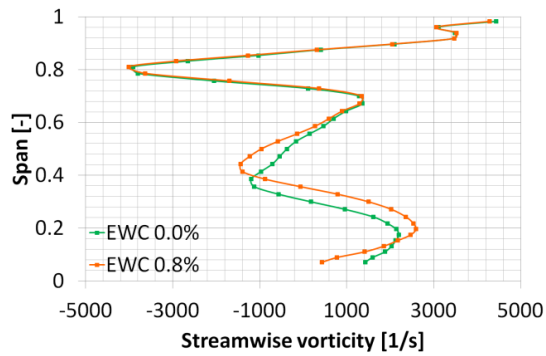

Figure 10: Time averaged and circumferentially mass weighted streamwise vorticity for the EWC case

When looking at the traverses with the lowest penetration depth of the rotor HPV (left side in Figure 11) one can see that the location of the core is about 5% span closer to the hub end wall in the case of EWC. Since this traverse comes from the region in the flow with the lowest interaction with the secondary flows from the upstream vane, this again proves the effectiveness of the end wall contouring to reduce the penetration depth of the rotor secondary flows – even at this injection rate of IR2=0.8%.

However, as the interactions with the secondary flows from the upstream vane become larger (right side in Figure 11) the rotor HPV increases the radial migration and now a different pattern in the interaction between the flow structures can be seen when comparing both end wall cases. Whereas the rotor exit flow field of the turbine with the contoured end walls shows only one distinct region of high unsteadiness at the hub vortex, the flow field of the cylindrical end walls shows two more distinct unsteady features at the hub with a zone of interaction between both. This could be the result of a more intensified merging of the suction side leg of the horseshoe vortex into the migrated pressure side leg for the case of the contoured end walls. There, the stronger interaction with the secondary flows from the upstream vane and cavity exit could cause a stronger lift-off of the suction side leg than in the case of the cylindrical end walls, losing the benefit of penetration depth of the contoured end wall by the time the interaction with the secondary flows and cavity exit flows becomes dominant.

Downloaded from https://asmedigitalcollection.asme.org/GT/proceedings-pdf/GT2014/45622/V02CT38A027/4228507/v02ct38a027-gt2014-26007.pdf by ETH Zuerich user on 17 October 2019

Copyright © 2014 by Siemens Energy, Inc.

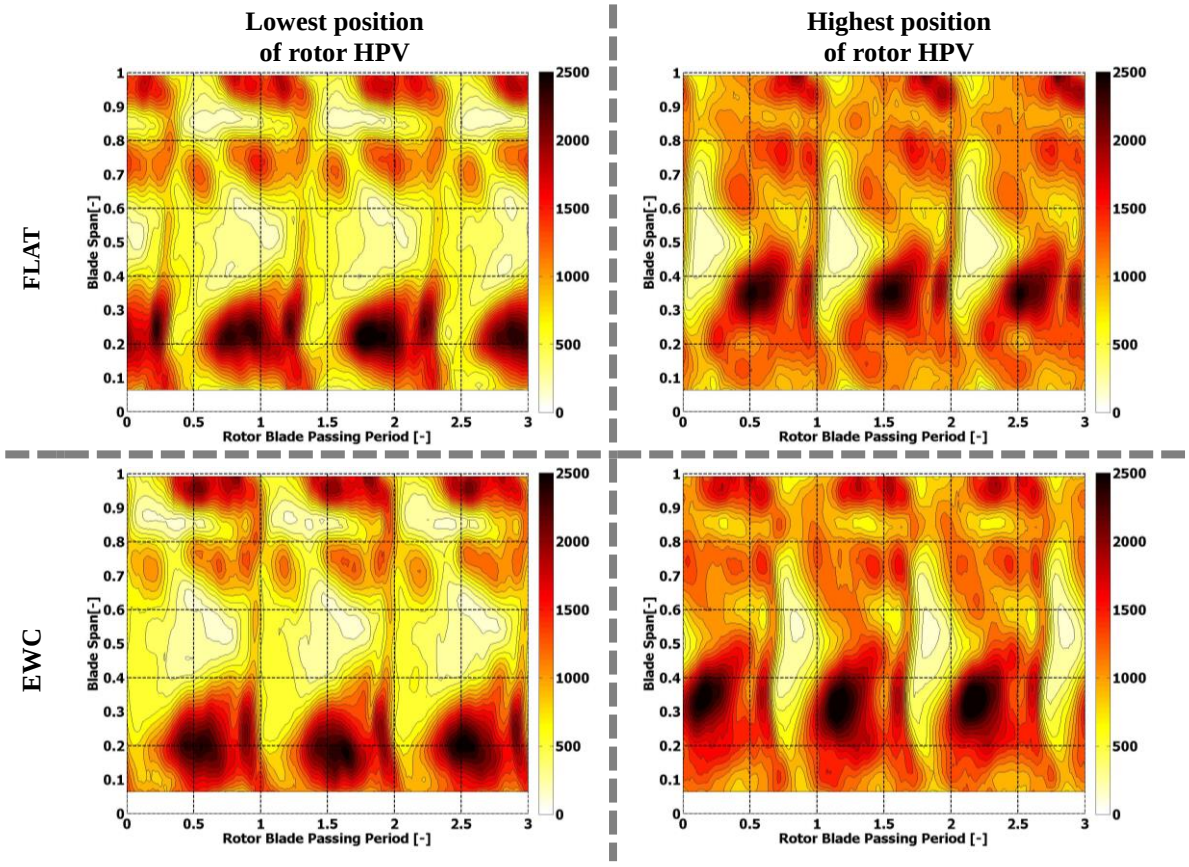

Figure 11: Span-time contours of rms(p_1') [Pa] at the rotor exit for the cylindrical end wall (top) and for the contoured end wall (bottom) for the radial traverses where the hub passage vortex core reaches the lowest (left) and highest (right) spanwise positions for the case with IR2=0.8% purge flow

Stator exit flow field

As seen in the rotor exit flow field, the lower robustness against purge flow of the stage with EWC originates from a loss in benefit after the interaction with the secondary flows from the vane. In the following, the vane's exit flow field will be described with a focus on the lower spanwise positions and the effect of the purge flow exit.

Time averaged measurements of total pressure by means of the pneumatic 4 HP show that the purge flow is already taking back performance benefit of the stage already at the exit of the stator. Here, the interaction between the purge flow and the main annulus flow is already captured and initiated, since the measurement plane is directly above the purge flow injection gap. In Figure 12 the circumferentially mass weighted normalized total pressure at the exit of the stator is depicted. The top diagram shows the comparison between the end walls at the injection rate IR2=0.8%, whereas the bottom diagram is showing the same flow quantity for the EWC case and the different injection rates tested.

The top diagram of Figure 10 shows a worse performance of the EWC for the spanwise positions below 12% span. In the EWC case the losses at the lowest accessible spanwise position are more than twice of those for the case with the cylindrical end walls, which integrally is not counterbalanced by the slight improvements of total pressure loss of the EWC case in the spans between 12% and about 40% span.

However, when considering the bottom diagram of Figure 12, the total pressure loss changes due to the purge flow variation show, that the large total pressure losses of the EWC case at those lowest accessible spanwise locations is introduced predominantly by the purge flow. This is concluded from the fact that the flow field of zero net purge flow does not show the sharp reduction of performance below 12% span.

Although no measurements at zero net injection exist for the cylindrical test case at this measurement location, the above diagrams strongly suggest that the performance deficit of the EWC case at IR2=0.8% is mainly coming as a result of the purge flow and cannot be attributed to the EWC per se. More specifically, the EWC design acts disadvantageously on the interaction and mixing mechanisms between the main annulus flow and the purge flow exit, which is already initiated and captured at this measurement location. This adverse effect is

Downloaded from https://asmedigitalcollection.asme.org/GT/proceedings-pdf/GT2014/45622/V02CT38A027/4228507/v02ct38a027-gt2014-26007.pdf by ETH Zuerich user on 17 October 2019

Copyright © 2014 by Siemens Energy, Inc.

considered to be a result of the strengthened turning of the end wall flow at the aft part of the stator passage as intended by the contoured end walls, which were not designed for the interaction with the purge flow.

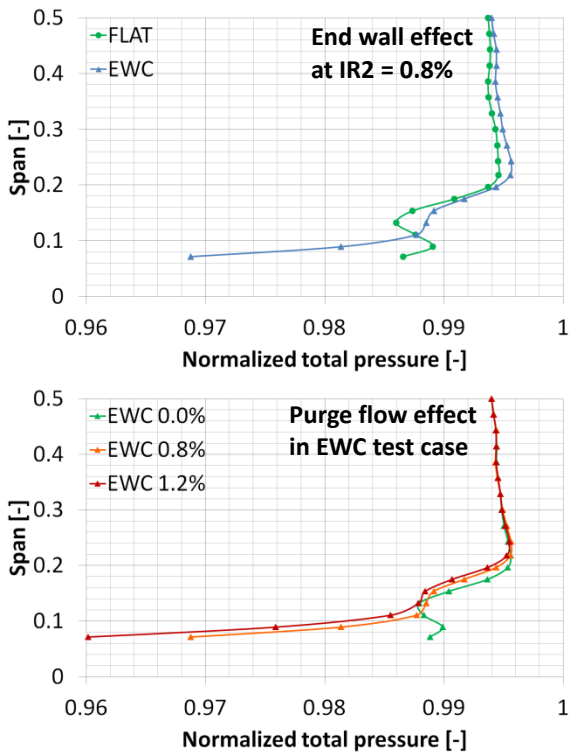

Figure 12: Time averaged and circumferentially mass weighted normalized total pressure at the exit of the stator comparing end walls at middle IR2=0.8% (top) and purge flow effect on EWC (bottom)

This conclusion is further confirmed by the 3D flow field at this measurement location. In Figure 13, the normalized total pressure at the lower spanwise positions is depicted for the case of the cylindrical end wall with IR2=0.8% on top, the contoured end wall with IR2=0.8% in the middle and the contoured end wall with IR2=0.0% at the bottom.

When looking at the end wall effect (and comparing top and middle diagrams) it becomes clear that the EWC design still holds the effectiveness for the convection and migration of the hub vortices, since the intensity of the hub passage vortex core is lower for the EWC case. However, similarly to the rotor exit flow field, the EWC design reduces the merging between the suction and pressure side legs of the horseshoe vortices, since they are seen as more distinct and more radially separated features in the case of the EWC.

However, to these two benefits on the convection and migration of the vortex legs there is an effect strongly counteracting found by the increased total pressure losses at the lower spanwise positions apart from the hub passage vortex. Since this secondary flow is not associated to the airfoils, it is a result of a strongly increased interaction mechanism between the contoured end walls and the purge flow injection.

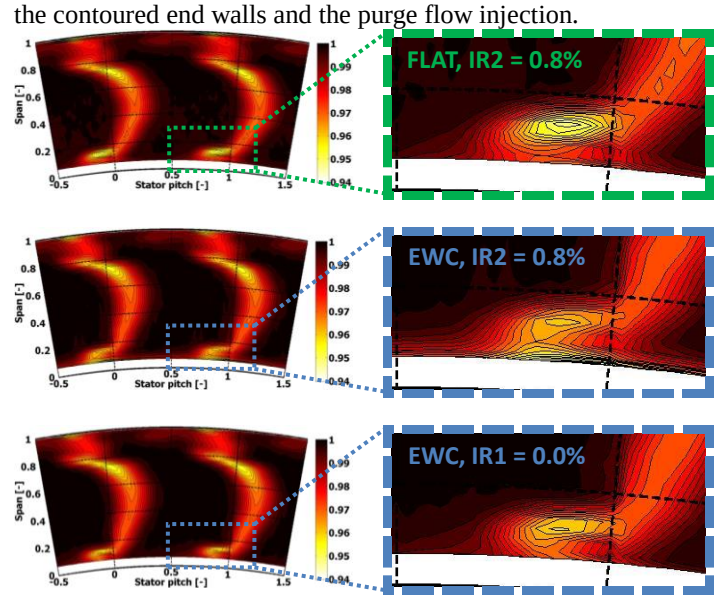

Figure 13: Time averaged normalized total pressure [-] at the exit of the stator for the cylindrical end wall at IR2=0.8% (top), for the contoured end wall at IR2=0.8% (middle) and for the contoured end wall at IR2=0.0% (bottom)

When looking at the purge flow effect on the EWC stage (and comparing middle and bottom diagrams) it becomes clear that this increased total pressure losses at low spans and even midpassage are considerably reduced when the purge flow is not active, confirming the above mentioned trend.

The time-resolved data at this measurement location gives a better insight into the different behaviour of the mixing of the purge flow with the main annulus flow for both tested end wall designs.

Figure 14 shows the circumference-time contour diagrams of the rms of the random part of the pressure signal as acquired by the FRAP at the lowest accessible spanwise position (6% span). The left diagram shows the flow field of the turbine with cylindrical end walls and IR2=0.8% whereas the middle diagram shows the flow field of the test case with EWC and IR2=0.8% and the right diagram for EWC with IR1=0.0%.

When focusing on the effect of the end walls (and comparing left and middle diagrams) the most salient difference is the overall higher level of unsteadiness for the EWC case, which is in agreement with the previously shown time-averaged increased total pressure loss. A further important difference can be found in the region influenced by the stator secondary flows, appearing as vertical features in this type of diagram in between -0.25 – 0.25 pitch. This is a region in the flow field which is predominantly influenced by the stator hub passage vortex and the trailing edge wake. It is observed that the region of high unsteadiness becomes a more distinctly inclined orientation for the case of the EWC stage, which means that the affected fluid is more driven by the rotor than by the stator.

Downloaded from https://asmedigitalcollection.asme.org/GT/proceedings-pdf/GT2014/45622/V02CT38A027/4228507/v02ct38a027-gt2014-26007.pdf by ETH Zuerich user on 17 October 2019

Copyright © 2014 by Siemens Energy, Inc.

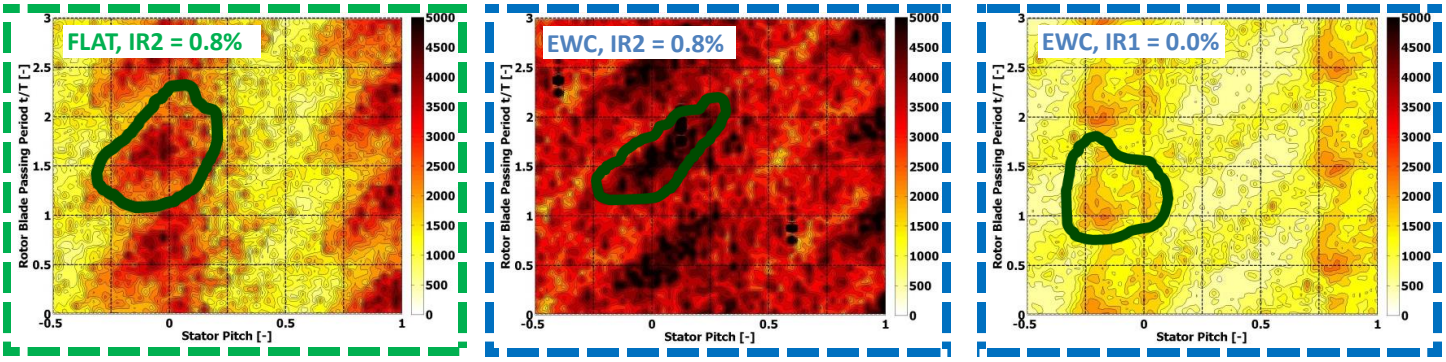

Figure 14: Circumference-time contours of rms(p_1') [Pa] at the exit of the stator for the cylindrical end wall at IR2=0.8% (left), for the contoured end wall at IR2=0.8% (middle) and for the contoured end wall at IR1=0.0% (right)

When focusing on the effect of purge flow on the EWC stage (and comparing middle and right diagrams), again, the most striking difference is the overall lower level of unsteadiness for the case with zero net purge flow injection, which is in agreement with the lower total pressure loss previously shown. However, with the absence of the net purge flow injection, the region affected by the secondary flows of the vane between -0.25 and 0.25 pitch become more vertical indicating that the dominance of the rotor on this region of the flow field is significantly reduced when the purge flow is not active. The rest of the flow field, between 0.25 and 0.75 pitch, and which is not in the influence area of the secondary flows of the vane has a minor signature of rotor dominated features, which can be caused by a rotor dominated pulsation of flow into and out of the cavity but will not be further discussed in this paper.

These results show that the sensitivity of the stage performance with respect to the purge flow injected, which is increased for the EWC case, is mainly dominated by the rotor HPV and is already initiated at the inlet of the rotor; more specifically in the interaction zone of the end wall flow and the exit of the purge flow.

Off-design sensitivity of the EWC

With the purpose of further giving an insight into the aerodynamic robustness of the end wall contouring design with respect to the purge flow and the off-design effect associated with it, both turbine stages have been tested under overall off-design conditions with constant purge flow injection rate of IR2=0.8%. The mass flow and the total inlet pressure of the turbine have been reduced simultaneously in order to achieve a reduction in rotor incidence by approximately 6°. The operating conditions are summarized in Table 3.

Experimental results not presented in this paper show that the impact of the loading reduction on the performance of the stator row is negligible, which allows to relate changes in the isentropic total-to-total stage efficiency to performance changes of the rotor row more specifically. In Figure 15 a time averaged comparison of the circumferentially mass averaged stage efficiency is given for the test case with cylindrical end walls on top and for the case with EWC at the bottom.

Table 3: Nominal and off-design operating points

	$\Delta i = 0°$	$\Delta i \approx -6°$
Speed [rpm]	2700	2700
Rotor capacity [kg $K^{1/2}$/s/bar]	152.7	137.5
Injection Rate IR [%]	0.8	0.8
Loading coefficient Ψ [-]	2.3	1.8

As expected, both test cases profit from unloading especially in the spanwise positions dominated by the secondary flows from casing and hub. However, the integral efficiency gain when unloading amounts to 1.2% for the EWC case and is 1/3 larger than the efficiency gain of +0.9% for the cylindrical end walls. The above radial distributions show that the increased gain in the EWC case originates from below midspan, which is the region affected by the EWC and purge flow interaction, as described before.

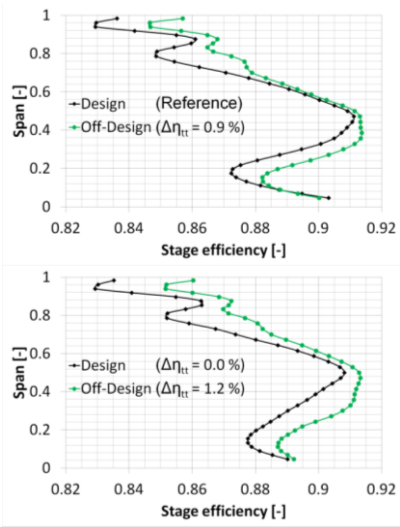

Figure 15: Time averaged and circumferentially mass weighted stage efficiency for the cylindrical end wall (top) and for the contoured end wall (bottom)

Copyright © 2014 by Siemens Energy, Inc.

Downloaded from https://asmedigitalcollection.asme.org/GT/proceedings-pdf/GT2014/45622/V02CT38A027/4228507/v02ct38a027-gt2014-26007.pdf by ETH Zuerich user on 17 October 2019

These measurements confirm that the tested EWC stage shows a higher sensitivity of the rotor performance with respect to changes in the incoming flow field to the rotor and with the presence of purge flow.

However, for the EWC case, also measurements with an increased stage loading coefficient and an increased rotor incidence have been taken. In Figure 16, the stage efficiency is plotted against the stage loading coefficient for the test cases discussed throughout this paper as well as for another test case, which was also not designed for the purge flow interaction and which features the same operating point, prismatic blading of the same family as the present test cases and cylindrical end walls.

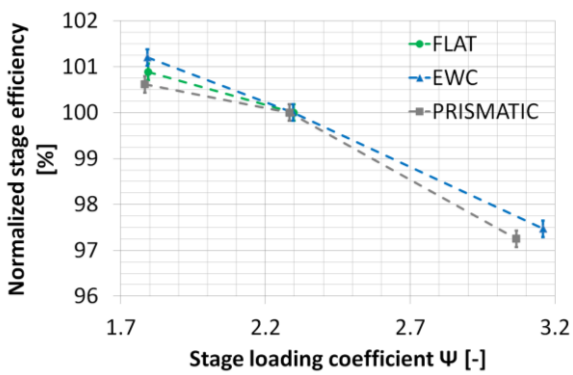

Figure 16: Normalized stage efficiency as a function of stage loading for the cylindrical and contoured end wall as well as for a stage with prismatic airfoils of the same vane and blade family

When comparing the sensitivity of the efficiency with respect to loading and unloading from the design point, both the EWC case and the prismatic case show the same trend: the sensitivity with respect to an increase in loading is higher than for a reduction of loading. Furthermore, the sensitivity of the test case with cylindrical end walls is in between the sensitivity of the EWC case and the prismatic case. Although no measurements for increased loading exist for the test case with cylindrical end walls, the above trends suggest that the sensitivity of the test case with cylindrical end walls for higher loadings is also bound between the sensitivities of the EWC case and the prismatic case. Based on that, it suggests that the EWC case has a better performance at higher loadings than the cylindrical test case. This thought is underpinned by the design intention of the end walls to perform slightly better at higher stage loadings. This can be attributed to a corrective effect of the increased rotor incidence: Since the end walls have not been designed for the purge flow interaction, the untreated purge flow exit introduces low momentum fluid close to the end walls and subsequently reduces the incidence on the rotor airfoil. An increase of rotor incidence by change in operating point could therefore counteract to the negative incidence effect of the purge flow and bring back the rotor incidence closer to the design point without purge flow and eventually act beneficially on the rotor end wall contouring performance.

CONCLUSIONS

The results presented in this paper are based on steady flow field measurements by high accuracy pneumatic probes as well as on time-resolved measurements by means of FRAP performed in a one-and-a-half stage research axial turbine. The tested configurations were equipped with blading representative for HP gas turbines under the presence of purge flow injection from the rotor upstream rim seal at injection rates of 0% representing zero net purge flow injection as well as 0.8% and 1.2% of the main annulus flow. Both turbine designs tested differ in the hub end walls, while one has cylindrical end walls the other one features contoured end walls. Since neither the airfoils nor the end walls were designed for the unsteady interaction mechanisms of the purge flow with the main annulus flow, these measurements intend to quantify the aerodynamic robustness of the contoured end walls against the purge flow. The main conclusions that are drawn include:

1. The stage efficiency measurements show an efficiency increase of +0.2% due to the use of end wall contouring for the case without net purge flow injection and confirm the predicted design intent and therefore prove the effectiveness of the end walls under operation at the design point.
2. However, the turbine designs perform differently, when they are operated under purge flow injection and its off-design effect. Although the impact of the contoured end walls versus the cylindrical end walls on the integral efficiency value is negligible for the injection rate of 0.8%, still the rotor exit flow fields differ, indicating a redistribution of mass flow due to the end wall contouring.
   The efficiency benefit at zero net purge flow injection is taken back as purge flow is introduced, and the contoured end wall case shows an efficiency sensitivity with respect to the purge flow, which amounts to -0.87% per percent of injected mass flow and which is more than 1/3 higher than in the stage with cylindrical end walls.
3. Time-resolved measurements at rotor exit reveal that the flow field of the turbine with the contoured end walls is characterized by an initiation of a detrimental time-dependent evolution of the rotor hub passage vortex, only at the point of time or vane-blade relative position, where the strongest interaction of the rotor HPV with the secondary flows from the upstream vane happens.
   The deteriorated performance of the contoured end wall stage under purge flow is already initiated at the inlet of the rotor, where the flow field is characterized by the interaction between the purge flow injection and the main annulus near end wall flow. There, due to the end wall contouring, the unsteadiness level is increased and the interaction between the purge flow and the secondary flows of the vane is more rotor-dominated in the case of the end wall contouring.

Downloaded from https://asmedigitalcollection.asme.org/GT/proceedings-pdf/GT2014/45622/V02CT38A027/4228507/v02ct38a027-gt2014-26007.pdf by ETH Zuerich user on 17 October 2019

Copyright © 2014 by Siemens Energy, Inc.

4. If an end wall contouring is to be designed for a stage operating under hub purge flow conditions, the findings reported in this paper suggest deriving one main design guideline: The results indicate to focus the design effort in the modeling of the highly unsteady rotor-stator-purge flow interaction and more specifically in the interaction zone of the purge flow and the main annulus flow already at the early most location where this complex interaction is initiated and which propagates onto the secondary flow evolution of the downstream rotor. For the current turbine tested, this region is the aft part of the stator hub end wall. Furthermore, investing design effort into a combined design of the end wall contouring and the exit geometry of the rim seal by any means for controlling radial and tangential angles of the purge flow exit either in the rotating or in the stationary environment are considered to have the potential of reducing performance deterioration.

ACKNOWLEDGMENTS

The authors gratefully acknowledge the permission of Siemens and MTU to publish the data and the financial and intellectual support during the measurements.

PERMISSION FOR USE

The content of this paper is copyrighted by Siemens Energy, Inc. and is licensed to ASME for publication and distribution only. Any inquiries regarding permission to use the content of this paper, in whole or in part, for any purpose must be addressed to Siemens Energy, Inc. directly.

NOMENCLATURE

Variables:

i	incidence angle	[°]
IR	injection rate	[%]
$\dot{m}$	mass flow	[kg/s]
M	torque	[Nm]
N	rotational speed	[rpm]
p	pressure	[Pa]
R	hub radius	[m]
T	temperature	[K]
U	local rotational speed	[m/s]
γ	isentropic coefficient	[-]
η	isentropic efficiency	[-]
μ	dynamic viscosity	[Pa s]
Π	pressure ratio	[-]
ρ	density	[kg/m^3]
φ	flow yaw angle	[°]
$\Phi = c_{ax}/U$	flow coefficient	[-]
$\psi = \Delta H/U^2$	loading coefficient	[-]
ω	angular frequency	[1/s]

Subscripts:

0	stagnation flow quantity
c	compressor
in	turbine inlet flow quantity
max	maximum
rel	relative frame flow quantity
tt	total-to-total

Abbreviations:

EWC	end wall contouring
FOR	frame of reference
FRAP	Fast Aerodynamic Response Probe
HP	hole probe
HPV	hub passage vortex
IP	intermediate pressure
NGV	nozzle guide vane

REFERENCES

[1] Rose, M. G., Harvey, N. W., Seaman, P., Newman, D. A. and McManus, D., 2001, "Improving the Efficiency of the TRENT 500 HP Turbine Using Non-Axisymmetric End Walls. Part II: Experimental Validation", Proceedings of ASME Turbo Expo 2001, 2001-GT-0505

[2] Harvey, N. W., Brennan, G., Newman, D. A. and Rose, M. G., 2002, "Improving Turbine Efficiency Using Non-Axisymmetric End Walls: Validation in the Multi-Row Environment and With Low Aspect Ratio Blading", Proceedings of ASME Turbo Expo 2002, GT-2002-30337

[3] Snedden, G., Dunn, D., Ingram, G. and Gregory-Smith, D., 2010, "The Performance of a Generic Non-Axisymmetric End Wall in a Single Stage, Rotating Turbine at On and Off-Design Conditions", Proceedings of ASME Turbo Expo 2010, GT2010-22006

[4] Schüpbach, P., Abhari, R. S., Rose, M. G., Germain, T., Raab, I. and Gier, J., 2010, "Improving Efficiency of a High Work Turbine Using Nonaxisymmetric Endwalls – Part II: Time-Resolved Flow Physics", Journal of Turbomachinery, Vol. 132, 021008 (10 pp.)

[5] Miyoshi, I., Higuchi, S. and Kishibe, T., 2013, "Improving the Performance of a High Pressure Gas Turbine Stage Using a Profiled Endwall", Proceedings of ASME Turbo Expo 2013, GT2013-95148

[6] Dunn, D., Snedden, G., von Backström, T. and Mdluli, M. P., 2013, "Unsteady Effects of a Generic Non-Axi-symmetric Endwall Contour on the Rotor of a 1½ Stage Low Speed Turbine Test Rig", Proceedings of ASME Turbo Expo 2013, GT2013-94961

[7] Hunter, S. D. and Manwaring, S. R., 2000, "Endwall Cavity Flow Effects on Gaspath Aerodynamics in an Axial Flow Turbine: Part I – Experimental and Numerical Investigation", Proceedings of ASME Turbo Expo 2000, 2000-GT-651

Downloaded from https://asmedigitalcollection.asme.org/GT/proceedings-pdf/GT2014/45622/V02CT38A027/4228507/v02ct38a027-gt2014-26007.pdf by ETH Zuerich user on 17 October 2019

Copyright © 2014 by Siemens Energy, Inc.

[8] Schrewe, S., Linker, C., Krichbaum, A. and Schiffer, H.-P., 2011, "Measurements of Rim Seal Mixing Processes in an Axial Two Stage Turbine", Proceedings of ISABE Conference, ISABE-2011-1720

[9] Jenny, P., Abhari, R. S., Rose, M. G., Brettschneider, M., Gier, J. and Engel, K., 2011, "Low-Pressure Turbine End Wall Design Optimisation and Experimental Verification in the Presence of Purge Flow", Proceedings of ISABE Conference, ISABE-2011-1717

[10] Ong, J. H. P., Miller, R. J. and Uchida, S., 2006, "The Effect Of Coolant Injection On The Endwall Flow Of A High Pressure Turbine", Proceedings of ASME Turbo Expo 2006, GT2006-91060

[11] Schuepbach, P., Abhari, R. S., Rose, M. G., Germain, T., Raab, I. and Gier, J, 2010, "Effects of Suction and Injection Purge-Flow on the Secondary Flow Structures of a High-Work Turbine", Journal of Turbomachinery, Vol. 132, 021021 (8 pp.)

[12] McLean, C., Camci, C. and Glezer, B., 2001, "Mainstream Aerodynamic Effects Due to Wheelspace Coolant Injection in a High-Pressure Turbine Stage: Part I – Aerodynamic Measurements in the Stationary Frame", Journal of Turbomachinery, Vol. 123, pp. 687-696

[13] Reid, K., Denton, J., Pullan, G. Curtis, E. and Longley, J., 2006, "The Effect Of Stator-Rotor Hub Sealing Flow On The Mainstream Aerodynamics Of A Turbine", Proceedings of ASME Turbo Expo 2006, GT2006-90838

[14] Regina, K., Abhari, R. S. and Kalfas, A. I., 2013, "Sensitivity of Purge Flow Effects to Different High Work Turbine Designs", Proceedings of ISABE Conference, ISABE-2013-1152

[15] Paniagua, G., Dénos, R. and Almeida, S., 2004, "Effect of the Hub Endwall cavity Flow on the Flow-Field of a Transonic High-Pressure Turbine", Journal of Turbomachinery, Vol. 126, pp. 578-586

[16] Regina, K., Kalfas, A. I. and Abhari, R. S., 2012, "Experimental Investigation of Purge Flow Effects on a High Pressure Turbine Stage", Proceedings of ASME Turbo Expo 2012, GT2012-69466

[17] Schuepbach, P., Abhari, R. S., Rose, M. G. and Gier, J., 2011, "Influence of Rim Seal Purge Flow on the Performance of an Endwall-Profiled Axial Turbine", Journal of Turbomachinery, Vol. 133, 021011 (10 pp.)

[18] Turgut, Ö. H. and Camci, C., 2013, "Influence of Leading Edge Fillet and Nonaxisymmetric Contoured Endwall on Turbine NGV Exit Flow Structure and Interactions With the Rim Seal Flow", Proceedings of ASME Turbo Expo 2013, GT2013-95843

[19] Rakenius, C., Schmid, G. and Schiffer, H.-P., 2013, "The Unsteady Effect of Contoured Endwalls on Purge Flow and Secondary Flow System in an Axial Turbine", Proceedings of ISABE Conference, ISABE-2013-1165

[20] Behr, T., Kalfas, A. I. and Abhari, R. S., 2007, "Unsteady Flow Physics and Performance of a One-and-1/2-Stage Unshrouded High Work Turbine", Journal of Turbomachinery, Vol. 129, pp. 348-359

[21] Kupferschmied, P., Köppel, P., Gizzi, W., Roduner, C. and Gyarmathy, G., 2000, "Time-resolved flow measurements with fast-response aerodynamic probes in turbomachines", Meas. Sci. Technol. 11, pp. 1036-1054

[22] Pfau, A., Schlienger, J., Kalfas, A. I. and Abhari, R. S., 2003, "Unsteady 3-dimensional flow measurement using a miniature virtual 4 sensor fast response aerodynamic probe (FRAP)", Proceedings of ASME Turbo Expo 2003, GT2003-38128

Downloaded from https://asmedigitalcollection.asme.org/GT/proceedings-pdf/GT2014/45622/V02CT38A027/4228507/v02ct38a027-gt2014-26007.pdf by ETH Zuerich user on 17 October 2019

Copyright © 2014 by Siemens Energy, Inc.